Ultralong Lifespan of SuperRedox Capacitor using Ti–doped Li$_3$V$_2$(PO$_4$)$_3$ Cathode with Suppressed Vanadium Dissolution

Journal:	*Journal of Materials Chemistry A*
Manuscript ID	TA-ART-10-2023-006240.R1
Article Type:	Paper
Date Submitted by the Author:	03-Dec-2023
Complete List of Authors:	Harada, Yuta; Tokyo University of Agriculture and Technology, Department of Applied Chemistry Okita, Naohisa; Tokyo University of Agriculture and Technology, Department of Applied Chemistry Fukuyama, Masahiro; Tokyo University of Agriculture and Technology, Department of Applied Chemistry Iwama, Etsuro; Tokyo University of Agriculture & Technology, Department of Applied Chemistry Naoi, Wako; K & W Inc., Naoi, Katsuhiko; Tokyo University of Agriculture and Technology, Department of Applied Chemistry

SCHOLARONE™
Manuscripts

ARTICLE

Ultralong Lifespan of SuperRedox Capacitor using Ti-doped Li$_3$V$_2$(PO$_4$)$_3$ Cathode with Suppressed Vanadium Dissolution

Yuta Harada[a], Naohisa Okita[a]*, Masahiro Fukuyama[a], Etsuro Iwama[a,b,c], Wako Naoi[d], and Katsuhiko Naoi[a,b,c]*

In this study, we successfully synthesized highly dispersed composites of multiwalled carbon nanotubes (MWCNTs). This was achieved by stoichiometrically substituting various metal ions, namely Ti^{4+}, Al^{3+}, and/or Mn^{2+}, into monoclinic Li$_3$V$_{2-x}$ M$_x$(PO$_4$)$_3$ (LVP), where X varies from 0 to 0.5. The substituted LVP materials, including Ti-, Al-, and Mn-LVP, consistently exhibited enhanced electrochemical performance, surpassing 10,000 cycles in cycling tests. Notably, Ti-LVP (X=0.1) displayed a remarkable capacity retention of 88.6% after 10,000 cycles. Our investigation entailed a comprehensive characterization of the electrochemical behavior of Ti-LVP over the entire doping range (X = 0–0.5). This characterization considered the crystal structure and its potential dependence on V-sites and Li-sites, along with their interplay with the proposed mechanism. Remarkably, a significant reduction (>50%) of vanadium dissolution was observed in immersion tests in polar solvents under extreme conditions with Ti-doped LVP. To gain further insights into this groundbreaking suppression behavior, we employed a combination of X-ray absorption fine structure (XAFS) analysis and precise molecular orbital calculations via the DV-Xα method. This approach unveiled a potential reduction in the ionicity of V^{3+} in V-O bonds within the bulk of LVP crystals and underscored surface interactions with electrodes and particles as contributing factors. The impact of suppressing parasitic reactions at the anode due to vanadium dissolution was evident in full-cell tests employing a configuration of Li$_4$Ti$_5$O$_{12}$/(1M LiPF$_6$/EC: DEC)/ Li$_{2.9}$V$_{1.9}$Ti$_{0.1}$(PO$_4$)$_3$, which demonstrated exceptional performance. Overall, the findings of this study hold significant promise for advancing the development of ultrafast and reliable energy storage technologies such as SuperRedox Capacitors, paving the way for a more sustainable and environmentally friendly future.

Introduction

The increasing demand for electric vehicles and renewable energy sources[1] has underscored the need for advanced batteries and supercapacitors(SCs) that prioritize safety and high-power performance characteristics.[2] SuperRedox Capacitor (SRC), based on pseudocapacitive/ultrafast battery-like positive and negative electrode materials, is a promising candidate for next-generation SCs with dramatically improved energy density compared to previous SCs without sacrificing high power density and long cycle time.[3] Among potential cathode materials, lithium vanadium phosphate (Li$_3$V$_2$(PO$_4$)$_3$: LVP) has emerged as a notable candidate. LVP offers superior safety features to conventional cathode materials such as LiCoO$_2$ and LiCo$_{0.33}$Ni$_{0.33}$Mn$_{0.33}$O$_2$ and boasts a high operating potential of 4.3 V, along with a respectable theoretical specific

capacity of 131 mAh g^{-1} resulting from the redox of V^{3+}/V^{4+} for a 2-electron reaction.[4] The 3-dimensional Li$^+$ diffusivity of LVP, approximately one order of magnitude higher than other polymorphs such as LiFePO$_4$: LFP, further enhances its appeal.[5,6] Adopting a nano-architecture electrode based on LVP is crucial to fully leverage its potential as a crystal material. However, this is challenging owing to LVP's inherently low electronic conductivity, typically ranging from 10^{-8} to 10^{-9} Ω^{-1} cm^{-1}.[7] Nonetheless, this limitation has been successfully addressed through composite synthesis by integrating conductive carbons, employing an innovative approach known as ultracentrifugation (UC).[8] This method dramatically reduces electrode impedance, enhancing the overall performance of LVP-based energy storage devices. Despite notable advancement, a significant issue remains: capacity degradation during prolonged cycles at full-cell operation. Our previous studies have confirmed that even minute quantities of vanadium ions, possibly in the order of a few ppm, are released from the LVP material into the electrolyte.[9] Interestingly, these dissolved V-species are predominantly observed in full-cell experiments, such as lithium titanate (LTO)//LVP cell, but are intriguingly absent in half-cell (Li//LVP) experiments. The migration of these vanadium ions to the LTO counter electrode catalytically accelerates deterioration, leading to the accumulation of a solid–electrolyte interphase (SEI) through electrolyte decomposition.[9] This chain-reaction failure mode is exclusively observable in full-cell tests

[a] Department of Applied Chemistry, Tokyo University of Agriculture & Technology, 2-24-16 Naka-cho, Koganei, Tokyo 184-8558, Japan
[b] Global Innovation Research Organization, Tokyo University of Agriculture & Technology, 2-24-16 Naka-cho, Koganei, Tokyo, 184-8588 Japan
[c] Advanced Capacitor Research Center, Tokyo University of Agriculture & Technology, 2-24-16 Naka-cho, Koganei, Tokyo 184-8558, Japan
[d] Division of Art and Innovative Technologies, K & W Inc., 1-3-16-901 Higashi, Kunitachi, Tokyo 186-0002, Japan
† E-mail: n-okita@go.tuat.ac.jp (N.O.), k-naoi@cc.tuat.ac.jp (K.N.)
Electronic Supplementary Information (ESI) available:
See DOI: 10.1039/x0xx00000x

and results in persistent capacity degradation over 1,000 cycles and beyond. [9,10] Similar phenomena have been observed in other transition-metal-based cathodes, including those containing vanadium, manganese, nickel, and cobalt, where a substantial amount of dissolved transition metal (TM) ions are released into the electrolyte. [11–15]

Several approaches have been adopted to reduce capacity degradation, such as the optimization of electrolyte composition [9,12] and the amount of additives [10,13,16] to suppress the reductive decomposition at the anode, as well as Li^+ pre-doping to minimize any shift of SOC. [3,17] However, these previous approaches have been ineffective in preventing the dissolution of TM ions. To mitigate TM dissolution more effectively, alternative strategies have been explored, including surface coatings designed to shield the cathode from direct exposure to the corrosive elements in the electrolyte, as reported previously. [18–20] Another approach involves cationic and anodic doping that modifies the TM-O bond within the cathode structure. [21,22] In the case of $LiMn_2O_4$, various compounds have been employed for surface coatings, ranging from oxides and lithiated metal oxides to fluorides, polymers, and phosphates. [23–30] However, surface coating poses challenges such as increased resistivity, interfacial mismatches, and a mandatory two-step procedure, rendering it unsuitable for LVP-based full cells that demand ultrafast operation. Regarding cationic and anodic doping, Gutierrez et al. conducted a comprehensive investigation into the electrochemical performance of $Li_{1.1}Mn_{1.8}M_{0.1}O_{4-\delta}F_\delta$ doped with various metals (Al, Ti, Cr, Fe, Co, Ni) and reported that these dopants effectively stabilize the cathode against attacks from polar molecules. [21]

Consequently, cationic doping of LVP holds the potential to enhance cycle performance in full cells by curbing vanadium dissolution without compromising the high-rate performance characteristic of LVP. The present study focuses on the stoichiometric preparation of monoclinic-structured TM-doped $LVP(Li_3V_{2-x}M_x(PO_4)_3)$ by varying the type of metals and the doping ratio X. We chose Ti^{4+}, Al^{3+}, and Mn^{2+} as the metal ions to be substituted. This choice is based on two main considerations: i) stoichiometric substitutions with vanadium in LVP [8,31–33]; ii) the different valence and electronegativity values of these selected metals (V^{3+} = 1.545, Ti^{4+} = 1.730, Al^{3+} = 1.513, Mn^{2+} = 1.343) [34] are expected to influence the formation of V-O bonds within the material. In addition, this study includes a comprehensive examination of the capacity retention of the synthesized $Li_3V_{2-x}M_x(PO_4)_3$ materials with X ranging from 0.1 to 0.5. Furthermore, an alternative and original approach using UC is proposed to prepare a nanocomposite that maximizes capacity retention and prolongs cyclability without sacrificing rate performance. Our unique approach overcomes the challenges associated with surface coating, achieving outstanding electrochemical performance surpassing that of any previously reported LVP. In the three metal-doped LVPs, Ti-doped LVP exhibited excellent cycle performance in a full cell. Ti-doped LVP not only modified V-O bonding in bulk LVP by replacing titanium with vanadium but also achieved nano-level modification of the LVP surface morphology, resulting in the suppression of vanadium dissolution from LVP. These two effects suppress the degradation mode caused by vanadium dissolution in the full cell. Overall, this study presents a novel approach to control the ionicity of transition metals in electrode materials by focusing on electronegativity, with the aim to suppress the dissolution of both transition metals and vanadium. The findings of this study may open new avenues to address challenges associated with TM dissolution and provide valuable insights for the design of electrode materials, leading to improved energy storage devices.

Experimental

Materials

NH_4VO_2 (99%, Kanto Chemical Co.), $LiCH_3COO$, and H_3PO_4 served as sources for V, Li, and PO_4, respectively. Additionally, citric acid ($C_6H_8O_7$) (99.5%, Sigma-Aldrich) and ethylene glycol (99%, Wako Pure Chemical Industries) were employed as chelating agents. The sources for Ti, Al, and Mn were $Ti[O(CH_2)_3CH_3]_4$ (95%, Wako Pure Chemical Industries), $Al(NO_3)_3 \cdot 9H_2O$ (99%, Wako Pure Chemical Industries), and $(CH_3COO)_2Mn \cdot 4H_2O$ (99%, Wako Pure Chemical Industries), respectively. Multiwalled carbon nanotubes (MWCNTs) with a specific surface area of 240 m^2 g^{-1} [35] were chosen as the precursor carbon matrix for entangling nanoscale $Li_3V_2(PO_4)_3$. Ultrapure water with a resistance of 17 Ω cm was used as a medium in the entire preparation scheme.

Material Synthesis

M(Ti, Al, and Mn)-doped $Li_3V_2(PO_4)_3$/MWCNT composites (Ti-LVP, Al-LVP, and Mn-LVP) were synthesized via UC, as previously described. [36] The preparation involved two solutions, A and B. For solution A, $LiCH_3COO$, NH_4VO_2, various metal ion sources, $C_6H_8O_7$, and ethylene glycol were dissolved in H_2O and mixed at a molar ratio of 3:1.9:0.1:2:8. For solution B, H_3PO_4 solution and MWCNT were mixed for 30 min using ultrasonication and subsequently treated by a first UC process for 5 min to form a blackish gel. Subsequently, after adding solution A to B, a second UC treatment was conducted for 5 min. The resulting mixture underwent a drying process at 130°C, followed by further annealing for 33 min (3 min of heating, 30 min of holding) at 800°C under a nitrogen flow, yielding LVP composite powder.

Material Characterization

The crystalline structure of M-doped LVP/MWCNT was characterized via X-ray diffraction (XRD) using a Rigaku SmartLab instrument. To determine the carbon weight ratio in composites, a thermal analysis was conducted in a synthetic air atmosphere (20% O_2, 80% N_2) using a thermogravimetry differential thermal analyzer (TG/DTA) from Seiko Instruments (TG/DTA6300). High-resolution transmission electron microscopy (HRTEM) with a Hitachi H9500 model was employed to investigate the detailed nanostructure features of the composites, including the LVP particle size distribution and

composite morphology with conductive carbons. To ascertain the surface and bulk composition of Ti-LVP, scanning transmission electron microscopy and energy-dispersive X-ray spectroscopy (STEM-EDX) were utilized. The STEM-EDX analysis was conducted using a Hitachi HD2700 instrument. X-ray photoelectron spectroscopy (XPS) was performed using a JEOL Ltd. JPS-9200 instrument equipped with an Al X-ray source, and this analysis was conducted without Ar etching. Before conducting scanning electron microscopy (SEM) observations and XPS characterization, the sample electrodes underwent thorough washing with diethyl carbonate (DEC) within a glove box in an Ar atmosphere with a controlled dew point. Time-of-flight neutron powder diffraction (NPD) measurements were performed at the iMATERIA (BL20) facility of the Japan Photon Accelerator Research Complex (J-PARC, Ibaraki, Japan) to obtain NPD patterns corresponding to 0.5–4.8 Å in d spacing. X-ray adsorption fine structure (XAFS) measurements at the V K edges for the composite were performed in transmission mode and conversion electron yield mode at the beamline the BL5S1 of Aichi Synchrotron Radiation Center (Aichi, Japan).

Electrochemical Measurement

2032 coin-type Li-metal half-cells were constructed, consisting of a negative Li metal electrode and a positive M-doped LVP/MWCNT electrode. Additionally, LTO/LVP full cells were assembled with negative LTO and positive M-doped LVP/MWCNT electrodes in laminate-type cells. The electrolyte was a mixture of ethylene carbonate and diethyl carbonate (EC:DEC = 1:1), containing 1.0 M of lithium hexafluorophosphate ($LiPF_6$). A 25 μm-thick monolayer polypropylene separator (Celgardμ2400, Celgard) served as the separator. Positive electrodes of M-doped LVP/MWCNT were prepared by mixing 90 wt.% of the composite and 10 wt.% of polyvinylidene difluoride (PVdF) in n-methyl pyrrolidone (NMP). Negative electrodes of LTO were prepared by mixing 70 wt.% of the sample, 20 wt.% of acetylene black, and 10 wt.% of PVdF in NMP. The mixture was coated on an etched-Al foil (current collector) and dried at 80 °C in a vacuum for 12 h. The loading masses of electrodes were 1.6 for LTO and 0.9 mg cm^{-2} for LVP. The capacity ratio of the anode (N) and cathode (P) was fixed to N/P = 2.5 for the full cell. Prior to cell assembly, electrodes were further dried at 120°C for 2 h under vacuum. Cells were assembled in a dry room (dew-point temperature <–40°C). Electrochemical preconditioning of LTO was conducted through charge–discharge cycling with an additional Li metal electrode in the full-cell laminated cells. The LTO preconditioning process included (i) constant-current constant-voltage (CC-CV) charging to a cut-off potential of 1.0 V vs. Li/Li$^+$ with a holding time of 1 h, (ii) resting for 24 h, (iii) CC-mode discharge to 3.0 V, (iv) CC-mode charge and discharge between 1.0–3.0 V vs. Li/Li$^+$ for 9 cycles, and (v) CC-mode charging to SOC 25%. Simultaneously, LVP underwent a similar precycling using another additional Li metal in the cell. The LVP preconditioning process included: (i) CC-CV charging to a cut-off potential of 4.3 V vs. Li/Li$^+$ with a holding time of 1 h, (ii) resting for 24 h, (iii) CC-mode discharge to 2.5 V, and (iv) CC-mode charge and discharge between 2.5–
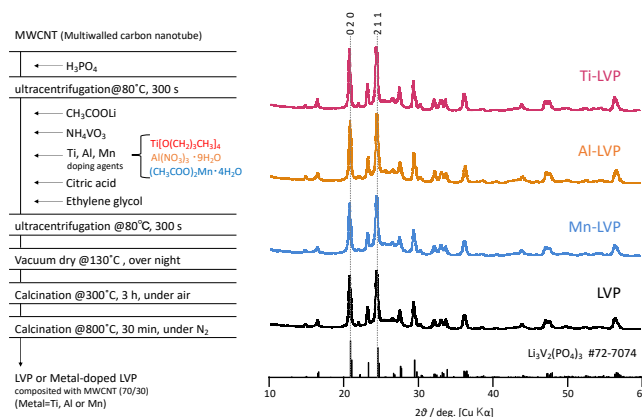
Fig.1 (Left) Preparation procedure for $Li_3V_2(PO_4)_3$ (LVP) and metal (Ti^{4+}, Al^{3+} or Mn^{2+})-doped LVP composited with MWCNT. **(Right)** XRD patterns for the respective composite samples of as-prepared LVP and as-prepared Ti-LVP, Al-LVP, and Mn-LVP. The LVP sample shows the main peaks responsible for plane (211) and plane (020) that are strictly indexed as monoclinic $Li_3V_2(PO_4)_3$ (S.G. P21/n $Li_3V_2(PO_4)_3$ indicated by JCPDS card no. 72-7074). They observed only the main LVP phase and no other impurity phase. Other three LVP samples doped (V-substituted with 0.5 atom% of metals), viz., Ti($Li_{2.9}V_{1.9}Ti_{0.1}(PO_4)_3$), Al($Li_3V_{1.9}Al_{0.1}(PO_4)_3$), and Mn($Li_{3.1}V_{1.9}Mn_{0.1}(PO_4)_3$) show exactly the same patterns as that of pristine LVP, indicating that the 0.5 atom%-substitution neither changes the monoclinic LVP main phase nor has any impurity phases such as oxides or other structures of phosphates.

4.3 V vs. Li/Li$^+$ for 9 cycles. Following the electrochemical preconditioning process, full cell packages were opened to remove Li metal electrodes. Thereafter, re-sealed full cells were cycled. The capacity of the LTO//LVP full cell was based on the mass of LVP active material (1C rate = 131.5 mA g^{-1} per LVP active material).

Molecular Orbital Calculation

The electron population density of chemical bonds in a model was determined via the DV-Xa cluster method. The model contains a limited number of atoms, *i.e.*, a cluster cut out of a crystalline solid, to characterize the properties of the bulk. A self-consistent charge method,[37], which establishes a Coulomb potential around a molecule through the combination of spherical atomic potentials, was employed to derive the Coulomb potential of the clusters. The electronic structure of the $Li_3V_2(PO_4)_3$ and $Li_{2.9}V_{1.9}Ti_{0.1}(PO_4)_3$ clusters is postulated, as detailed in the Results and Discussion section. To enhance the accuracy of calculations, the model was constructed with vanadium, the element of interest, positioned at the center of the cluster. The changes in net charge (NC) and bond overlap population (BOP) between vanadium or titanium and oxygen in the LVPs were computed. The NC and BOP parameters are indexes of the ionicity and covalency of the chemical bonds, respectively.[38,39]

Results and Discussion

Cycle characteristics in a full cell of LVP substituted with various metal ions

The detailed synthesis scheme, depicting the substitution of each heterogeneous metal ion, is illustrated in Fig. 1 (left). The authors have been synthesizing ultrafast materials utilizing UC
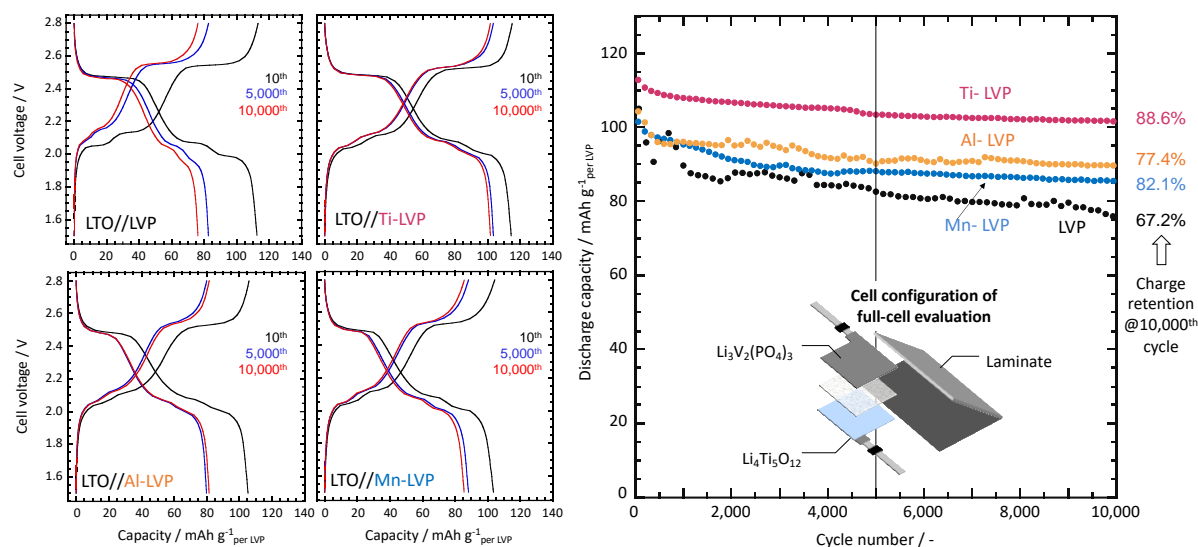
Fig.2 (left) Electrochemical responses for the four samples represented as the charge–discharge characteristics of full-cells: $Li_4Ti_5O_{12}$(LTO)//(pristine LVP or transition metal(Ti^{4+}, Mn^{2+}, and Al^{3+})-LVPs) at the early stage of cycling (@10th cycle). For both charging and discharging, all the curves show the same characteristics as those for LTO//LVP. The LTO//LVP cell showed drastic decay in capacity from the initial 10th cycle up to the 5,000th cycle and thereafter. Among all, the LTO//Ti-LVP cell showed the least drop in discharge capacity retention across the 10,000 cycles tested. The retention-decreasing rate is the same for others, viz., LTO//Al-LVP, LTO//Mn-LVP after 5000 cycles. Owing to the fixed N/P ratio of 2.5, indicating an abundant anode supply, the cathodic characteristics are highlighted. (right) The test was conducted as a full-cell employing an abundant (2.5 times) LTO anode, following the methodology of our previous study.[8] This setup enables emphasizing the cathode properties. Furthermore, this test enables the detection of any adverse effect on the LTO anode as a result of prolonged cycling, in this case, spanning up to 10,000 cycles. [Conditions for full-cell evaluation]: Positive electrode (PE): LVP: MWCNT: PVDF = 63: 27: 10, Negative electrode(NE): LTO: AB: PVDF = 70: 20: 10, Electrolyte: 1.0 M $LiPF_6$ / EC: DEC (1:1 vol.), Voltage range: 1.5–2.8 V, Charge/Discharge@10C/10C (1C = 131.5 mA $g^{-1}_{per\ LVP}$), Temperature: 25 °C

treatment, transforming battery materials into capacitor-like materials, yielding exceptional electrochemical responses. One example includes UC-derived LVP/MWCNT composites, where nanosized LVP precursors have been built up at the surface/interstices of a nanocarbon network, exhibiting hyperdispersed conditions. Typically, these composites demonstrate excellent rate capability, retaining a substantial capacity density of 83 mAh g^{-1} @480C-rate[8] in a half-cell configuration. In our ongoing research, we aim to delve deeper into this ultrafast family of LVPs utilizing UC composites as a potent tool. We explore fine-tuning various calcination conditions, such as temperature/duration and other parameters, to introduce additional elements. This approach is anticipated to yield unexpected electrochemical characteristics surpassing those of pristine LVP. Recognizing the critical issue of vanadium dissolution in full cells using LVP as a cathode, we hypothesized that modifying the V-O bond in the LVP crystal structure by substituting other metal ions for vanadium could be an effective strategy. We selected Ti^{4+}, Al^{3+}, and Mn^{2+} as the metal ions for substitution. A reagent, namely $Ti[O(CH_2)_3CH_3]_4$, $Al(NO_3)_3 \cdot 9H_2O$, or $(CH_3COO)_2Mn \cdot 4H_2O$, was introduced before the second UC, with a substitution ratio of 5 atom%, respectively. Fig. 1 (right) presents the XRD patterns of LVP/MWCNT composites (LVP, Ti-LVP, Al-LVP, and Mn-LVP) with the doping of different metal ions. Notably, the XRD patterns of all four composites were indexed as monoclinic LVP without any impurity phase peaks such as oxides or other structures of phosphates. To ascertain the residual weight ratio of the composite carbon, TGA analysis was conducted in a synthetic air atmosphere (Fig. S1). The carbon content in these composites was estimated based on the weight decrease

around 450 °C derived from the carbon combustion. The carbon content in the composite closely matched the preparation ratio for all composites: 70 wt% (LVP), 70 wt% (Ti-LVP), 70 wt% (Al-LVP), and 66 wt% (Mn-LVP). Combining the XRD and TGA results, we successfully synthesized all samples as high-purity LVP/carbon composites with the desired carbon contents. The lattice parameters, calculated by Rietveld refinement, indicated an increased lattice volume for Ti-LVP and Mn-LVP and a decreased volume for Al-LVP (Table S1). These findings suggest the successful substitution of metal ions for vanadium in monoclinic LVP, regardless of the specific metal ion used.

We aim to assess any enhancements in electrochemical performance, particularly in terms of cyclability, in full cells utilizing lithium titanate ($Li_4Ti_5O_{12}$: LTO) as the anode. LTO was chosen as the anode for two key reasons: First, its relatively high reaction potential, and second, its outstanding rate performance. Given that the reaction potential of LTO is 1.55 V vs. Li/Li$^+$, we can attribute any observed electrolyte decomposition solely to the catalytic effect of dissolved vanadium[9]. This configuration facilitates the detection of any potential adverse effects of cathode materials, such as vanadium dissolution due to extended cycling, encompassing up to 10,000 cycles. LTO also facilitates rapid Li intercalation, rendering it an ideal anode material for evaluating the electrochemical properties of LVP in fast charge–discharge operations. Representative charge–discharge characteristics are depicted in Fig. 2 (left). During the 10th cycle, all full cells exhibited three plateaus at approximately 2.0, 2.1, and 2.51 V, characteristic of the lithium intercalation/deintercalation reactions with LVP at 0.5, 0.5, and 1.0 equivalents, respectively. The capacities of each composite at the 10th cycle and rate of

10C were as follows: 112.6 mAh g^{-1} (LVP), 114.3 mAh g^{-1} (Ti-LVP), 105.4 mAh g^{-1} (Al-LVP), and 103.5 mAh g^{-1} (Mn-LVP). Notably, Al-LVP and Mn-LVP exhibited lower capacities than LVP, possibly due to the formation of inactive redox sites in these composites as a result of vanadium substitution with these metal ions. When vanadium was replaced with inert metal ions, the capacity decreased by approximately 5% (7 mAh g^{-1}), which is roughly consistent with the capacity reduction observed in Mn-LVP and Al-LVP relative to LVP. In contrast, Ti-LVP demonstrated a higher capacity than LVP. This result aligns with a previous study by Wang et al., who reported improved rate capacities of Ti^{4+}-substituted LVP due to enhanced Li diffusion through the formation of Li vacancies[27,40,41]. Therefore, the higher capacity observed in Ti-LVP than LVP can be attributed to improved rate properties resulting from Ti^{4+} substitution and the formation of Li vacancies.

The primary focus of this study lies in investigating the long-term cyclability of a series of LVP cathode materials, where V^{3+} is replaced by different metal ions such as Ti^{4+}, Al^{3+}, or Mn^{2+} as shown in Fig.1. The charge–discharge profiles for the 5,000th and 10,000th cycles indicated a decrease in capacity in all full cells compared with the 10th cycle. In the LVP full cell, the capacities were 83 mAh g^{-1} and 75 mAh g^{-1}, with 74% and 67.2% capacity retention at the 5,000th and 10,000th cycle, respectively, indicating a continuous decrease in capacity. The plateau around 2.0 V in the discharge curve of the non-doped LVP full cell almost disappeared, suggesting a shift in the state-of-charge (SOC) of the LVP cathode.[10] In contrast, Ti-LVP, Al-LVP, and Mn-LVP exhibited capacities of 104 mAh g^{-1}, 80 mAh g^{-1}, and 85 mAh g^{-1}, respectively, with a capacity retention of 88.6%,
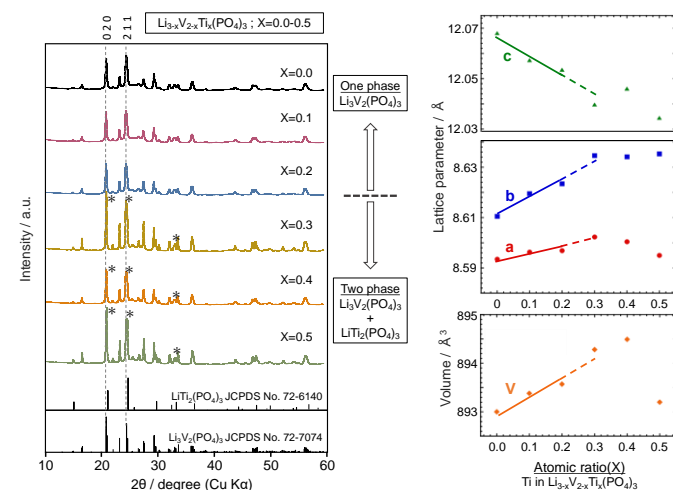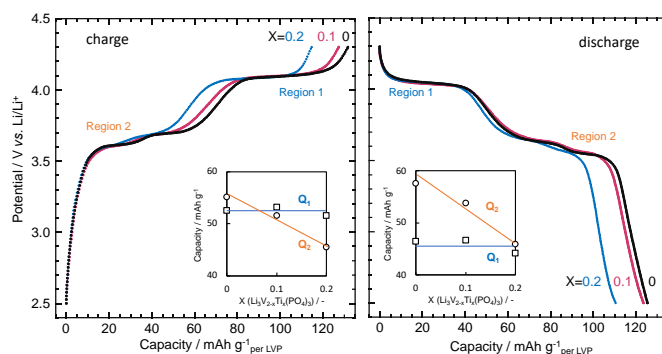

Fig.4 The intercalation mechanism can be effectively represented through charge–discharge curves at a rate of 1C for lithium-ion cells using the Li//[Li$_{3-x}$V$_{2-x}$Ti$_x$(PO$_4$)$_3$/MWCNT] configuration. These curves are extracted from the initial state (2nd cycle) for three distinct samples with X values of 0, 0.1, and 0.2. Our specific focus lies on the cathode behavior observed in two distinct potential regions, denoted as Region 1 (indicated by the blue bar) and Region 2 (indicated by the orange bar). As illustrated in the lower inset, we have plotted the capacities for Regions 1 and 2, which are tabulated in the upper inset, against the parameter X (representing Li$_3$V$_{2-x}$Ti$_x$(PO$_4$)$_3$) for X values of 0, 0.1, and 0.2. In Region 1, the capacities exhibited by the three discharge curves remain relatively stable with minor variations in response to changes in the titanium substitution ratio (X). Conversely, in Region 2, the curves follow distinct trajectories, with capacities decreasing as the titanium doping level (X) increases.

77.4%, and 82.1% at the 10,000th cycle, showcasing an improvement in cycle performance. In Ti-LVP, Al-LVP, and Mn-LVP full cells, the overall plateau length in the charge–discharge curves slightly decreased, implying minimization in capacity degradation due to SOC shift. Consequently, in the subsequent sections, we discuss the factors responsible for suppressing vanadium dissolution and the mechanisms underlying the enhanced cycle performance observed in Ti-LVP full cells exhibiting the highest cycle performance among the M-doped LVPs.

Characterization of Ti-LVP and suppression of vanadium dissolution

To explore the factors contributing to the improved full-cell performance of Ti-LVP, we initially synthesized Li$_{3-x}$V$_{2-x}$Ti$_x$(PO$_4$)$_3$ materials with varying stoichiometric ratios of Ti^{4+} (X = 0, 0.1, 0.2, 0.3, 0.4, 0.5) and examined the changes in the crystal structure with the amount of Ti^{4+} substitution (X). The XRD patterns of each composite with X ≤ 0.2 exclusively showed the peak corresponding to monoclinic Li$_3$V$_2$(PO$_4$)$_3$ (S.G. $P2_1$/n Li$_3$V$_2$(PO$_4$)$_3$, as indicated by JCPDS card no. 72-7074), and no other peaks were observed (Fig. 3, left). However, for X > 0.3, peaks corresponding to both monoclinic Li$_3$V$_2$(PO$_4$)$_3$ and NASICON LiTi$_2$(PO$_4$)$_3$ (S.G. R3-c LiTi$_2$(PO$_4$)$_3$, as indicated by JCPDS card no. 72-6140) were detected. For each composite, lattice constants were calculated by Rietveld analysis. For X < 0.2, a, b, and lattice volumes (V) were observed to increase with X, while c decreased with an increase in X. (Fig.3 (right)) Conversely, for X ≥ 0.3, no apparent correlation between any of the lattice constants and X was observed. These results suggest that Ti^{4+} is effectively introduced into LVP below X = 0.2, while above X = 0.3, a limited amount of Ti^{4+} is introduced into LVP, along with the formation of the impurity NASICON LiTi$_2$(PO$_4$)$_3$. Despite the ionic radius of Ti^{4+} (0.604 Å) being smaller than that of V^{3+} (0.64
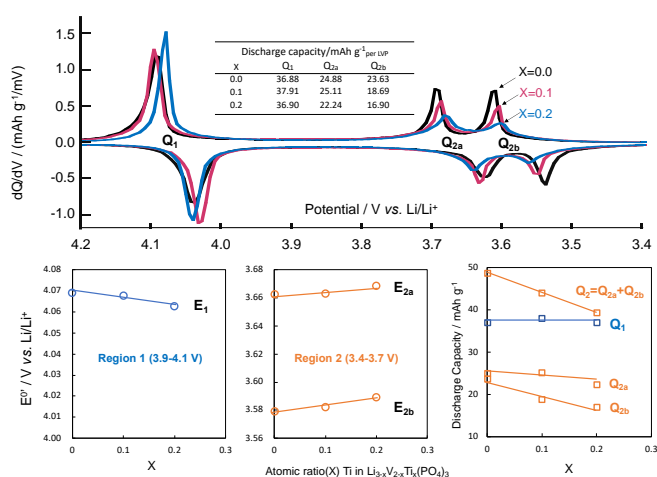

Fig.3 (Left) XRD patterns for the titanium-substituted Li$_{3-x}$V$_{2-x}$Ti$_x$(PO$_4$)$_3$/MWCNT composites with different atomic ratios (X) ranging from 0 to 0.5. All samples show the main peaks responsible for planes (211) and (020) that are strictly indexed as monoclinic Li$_3$V$_2$(PO$_4$)$_3$ (S.G. P21/n Li$_3$V$_2$(PO$_4$)$_3$, as indicated by JCPDS card no. 72-7074). In the XRD patterns with X ≤ 0.2, the main phase is monoclinic LVP, and no extra reflections for impurities are observed. When the substitution ratio is large (X = 0.3, 0.4, and 0.5), new peaks appear at 2θ = 20.62, 24.38, and 33.35° (denoted as asterisks*), corresponding to a possible impurity of LiTi$_2$(PO$_4$)$_3$ as indicated by JCPDS card no. 72-6140). (Right) Based on Rietveld refinement, the lattice parameters (a, b, c, and V) have been defined as a function of X (in Li$_{3-x}$V$_{2-x}$Ti$_x$(PO$_4$)$_3$/MWCNT (0 ≤ X ≤ 0.5)). Within the regions corresponding to X= 0–0.2, the values of a, b, and lattice volume (V) increase proportionally with X, while the c value decreases. Following Vegard's law, Ti^{4+} stoichiometrically substitutes V^{3+} in LVP crystals with smaller X ranges ≤0.2.

Fig.5 Observed $E^{0'}$ for $Li_{3-x}V_{2-x}Ti_x(PO_4)_3$ with X = 0.0, 0.1, and 0.2 in Region 1 (E_1) and Region 2 (E_{2a} and E_{2b}). E_1 decreases with increasing titanium substitution (X). E_{2a} and E_{2b} increase with X. The discharge capacities around respective potentials have been integrated/calculated as Q_1, Q_{2a}, and Q_{2b}, as tabulated in the inset of the upper view graph. Q_1 is considerably changed against X, while Q_{2a} and Q_{2b} decrease with X with different proportionality constants shown in the viewgraph (bottom right). More precisely, the slopes (dQ/dX) are -13.2 and -33.7 for Q_{2a} and E_{2b}, respectively.

Fig.6 Neutron diffraction of $Li_3V_2(PO_4)_3$ and $Li_{2.9}V_{1.9}Ti_{0.1}(PO_4)_3$ and Rietveld fit. Experimental (red), calculated (blue), and difference(green) curves are shown. The *hkl* positions (|) are marked for $Li_3V_2(PO_4)_3$ and $Li_{2.9}V_{1.9}Ti_{0.1}(PO_4)_3$, along with the accompanying difference curve below. The deduced crystal structure for $Li_3V_2(PO_4)_3$ and $Li_{2.9}V_{1.9}Ti_{0.1}(PO_4)_3$ is the result of Rietveld fitting based on neutron diffraction. In $Li_{2.9}V_{1.9}Ti_{0.1}(PO_4)_3$, titanium selectively replaces vanadium at the V(1) site, accompanied by a reduction in lithium occupancy at the Li(2) site.

Å), the a- and b-axes of the structure parameter increased. This could be attributed to a decrease in Li^+ ions. In Ti-LVP, the introduction of Ti^{4+} may lead to a decrease in Li+ for charge compensation. In the crystal structure of LVP, lithium is distributed along the ab-plane[42,43]. Therefore, the structure along the c-axis direction is expected to shrink and decrease as the Li^+ content decreases. However, this reduction in the c-axis direction could lead to a closer distance between adjacent V-V ions along the c-axis direction, potentially resulting in electrostatic repulsion. Consequently, the axes of the VO_6 octahedra in the c-axis direction might experience slight displacement, causing the structure to expand in the ab-plane direction and leading to an increase in the a- and b-axes.

To elucidate the impact of substituting vanadium with Ti^{4+} in LVP, charge–discharge tests were performed on half cells at a rate of 1C for different ratios of Ti^{4+} substitution (X = 0, 0.1, and 0.2), with no impurities detected (Fig. 4). The charge capacities were 125, 122.5, and 109 mAh g^{-1}, and the discharge capacities were 122.5, 122, and 110 mAh g^{-1} for X = 0, 0.1, and 0.2, respectively. These results indicate that charging and discharging proceed reversibly in all composites (X = 0, 0.1, and 0.2). Furthermore, decreasing capacities were observed with increasing X value, indicating successful substitution of Ti^{4+} for V^{3+}. The charge–discharge curves for the samples with X = 0, 0.1, and 0.2 exhibited plateaus in region 1 (3.9–4.2 V vs. Li/Li^+) and region 2 (3.5–3.8 V vs. Li/Li^+). The plateau in region 2 is further divided into two plateaus, a characteristic feature of LVP.[7,44,45] The plateaus in the two potential regions of LVP are attributed to the different vanadium sites that react at each potential. LVP with $P2_1/n$ space group has two distinct vanadium sites, V(1) and V(2). During the charging process, vanadium at the V(1) site is initially oxidized from V^{3+} to V^{4+} in the low-potential region 2, while vanadium at the V(2) site is oxidized from V^{3+} to V^{4+} in the high-potential region 1 (Fig. S2). To analyze this further, the capacities of each region, denoted as Q_1 and Q_2, were calculated
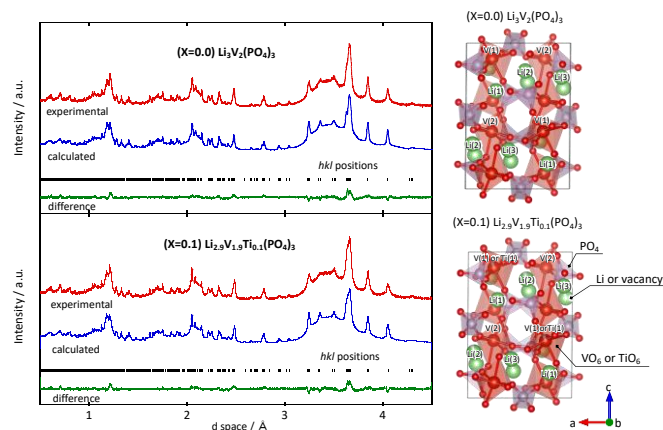
(Fig. 4 inset). It was observed that the value of Q_1 remained constant regardless of the increasing X, while Q_2 decreased with increasing X. This outcome suggests that vanadium at the V(1) site, which occurs in redox reactions in region 2, is selectively replaced by Ti^{4+}.

The dQ/dV plots illustrated in Fig. 5 are derived from the charge–discharge curves presented in Fig. 4. Peaks observed in the dQ/dV plots occurred during the charge and discharge processes within the potential ranges of 4.1–4.0, 3.7–3.6, and 3.6–3.5 V vs. Li/Li^+. These peaks are denoted as E_1, E_{2a}, and E_{2b} in Fig. 5, representing the average reaction potentials of each peak. E_1 slightly decreased while E_2 slightly increased with increasing titanium substitution (X). This change is correlated with the electron density around the V-O bond. In polyanionic cathode materials such as LVP, the inductive effect of the highly covalent P-O bond reduces the electron density around the V-O bond, resulting in an ionic V-O bond with a high reaction potential. Thus, the V-O bond associated with the V(1) site, where redox occurs at E_2 with an increase in Ti^{4+} substitution, becomes more ionic. Conversely, the V-O bond related to the V(2) site, where redox occurs at E1 with a decrease in Ti^{4+} substitution, becomes less ionic. This is attributed to the suppression of the inductive effect of PO_4 units by Ti^{4+}, which has a higher electronegativity than V^{3+} (V^{3+} = 1.545, Ti^{4+} = 1.730). Focusing on the discharge capacity, the capacity in region 1 (Q_1) remained constant with increasing Ti^{4+}. However, the capacities (Q_{2a} and Q_{2b}) in region 2 decreased with increasing Ti^{4+} in LVP, indicating a selective substitution of Ti^{4+} into the V(1) site. The redox of $V^{3+/4+}$ at the V(1) site is induced by the insertion/desertion of Li at the Li(2) site, one of the three Li sites of LVP[7,46]. Therefore, substituting Ti^{4+} for V^{3+} at the V(1) site is expected to decrease the occupancy of Li at the Li(2) site due to charge compensation. This vacancy causes a decrease in the capacities (Q_{2a} and Q_{2b}) in region 2 but enhances Li diffusivity, resulting in improved rate performances.

The results of Rietveld refinement by neutron diffraction analysis (Fig. 6) support the selective substitution of Ti^{4+} into the V(1) site, as suggested by electrochemical measurements. The observed neutron diffraction peaks of LVP and Ti-LVP can be indexed by a monoclinic $Li_3V_2(PO_4)_3$. Lattice parameters, atomic positions, and occupancies, including Li and expected vacancy sites for Ti-LVP, were determined through Rietveld refinements on the neutron diffraction data, as shown in Table S2. The obtained stoichiometry of the Ti-LVP crystal structure was $Li_{2.9}V_{1.9}Ti_{0.1}(PO_4)_3$. Ti^{4+} was present at the V(1) site, whereas vacancies were only at the Li(2) site to compensate for the valence. Combining the results of charge–discharge tests and neutron diffraction analysis, the charge–discharge of $Li_{3-x}V_{2-x}Ti_x(PO_4)_3$ is expected to proceed as follows (Fig. S3). At high potentials (3.9–4.1 V vs. Li/Li^+) in region 1, the redox of $V^{3+/4+}$ occurs at the V(2) site. The redox potential E_1 of vanadium at the V(2) site decreases because of a reduction in the inductive effect due to Ti^{4+} substituting the V(1) site. In contrast, at low potentials (3.4–3.8 V vs. Li/Li^+) in region 2, redox of $V^{3+/4+}$ occurs at the V(1) site. In this region, the capacity during charging and discharging decreases, and the peaks corresponding to potentials E_{2a} and E_{2b} decrease in the dQdV plot.

TEM observation was performed to examine the particle size and morphology of $Li_{2.9}V_{1.9}Ti_{0.1}(PO_4)_3$/MWCNT (X = 0.1) composites (Fig. 7 (a)). Nano-LVP particles (approximately 100 nm) were entangled in a matrix of MWCNTs. TGA measurements showed that the combustion temperature of carbon decreased in $Li_{2.9}V_{1.9}Ti_{0.1}(PO_4)_3$/MWCNT, suggesting a direct bonding between the dangling bonds of the nano-LVP crystal and the functional groups on the carbon surface, as reported previously.[8] However, no peaks corresponding to V-C or P-C bonds were observed in XPS measurements (Fig. 7 (c)). These results indicate that the obtained materials are a composite of LVP and MWCNT phases, including direct C-O-V and C-O-P bonds formed by the nano-LVP crystal and the functional groups on the carbon surface.
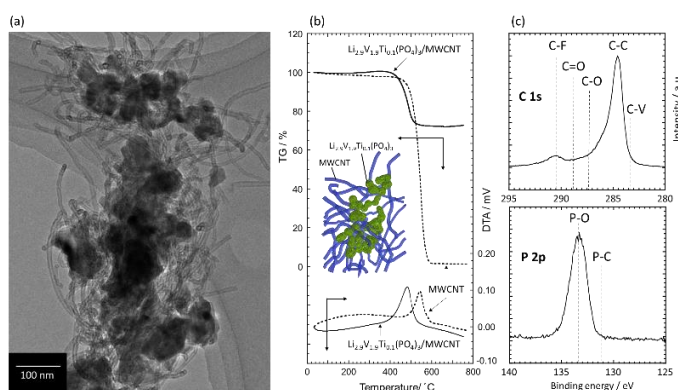

Fig.8 TEM images and the electron diffraction (ED) of $Li_{3-x}V_{2-x}Ti_x(PO_4)_3$/MWCNT composites for X = 0.0 (upper) and 0.1 (lower). The figure compares those two key features before and after the immersion of each sample into hot water (60 °C ; 47 h). After immersion in hot water, the pristine LVP (X = 0.0) particles completely disappear, and only MWCNTs are observed; moreover, the absence of diffraction spots in ED indicates that the crystal particles are possibly dissolved. In contrast, Ti-substituted LVP (X = 0.1) particles are observed even after immersion in hot water, and diffraction spots are also observed in ED. In contrast, at X = 0.1, LVP particles are observed even after immersion in warm water, and diffraction spots are observed even in ED.

To obtain evidence of the prevention of dissolution of vanadium into polar solvents by Ti-LVP, which leads to capacity degradation in full cells, $Li_{3-x}V_{2-x}Ti_x(PO_4)_3$/MWCNT composites for X = 0.0 and 0.1 were tested for their solubility in hot water at 60 °C for two days. Here, the immersion testing in hot water, which is a highly reactive polar solvent, is a harsh condition for these samples. To quantify the amount of vanadium dissolved, ICP-MS measurements were performed on the filtrate resulting from the soaking test (Fig. 8(b)). In LVP (X = 0.0), the amount of vanadium in the filtrate was 15.15 mg, corresponding to 86.57% of vanadium in as-prepared LVP dissolved from the crystals. Only MWCNTs were observed in the TEM images of LVP after immersion in hot water, with the disappearance of the diffraction spots in the ED corresponding to the LVP. In contrast, only 6.15 mg of vanadium was found in the

Fig. 7 (a) TEM images of the synthesized $Li_{2.9}V_{1.9}Ti_{0.1}(PO_4)_3$/MWCNT (x = 0.1) composites. (b) Thermogravimetric analysis (TGA) curves for $Li_{2.9}V_{1.9}Ti_{0.1}(PO_4)_3$/MWCNT (x = 0.1) composites (solid line) and MWCNT (dotted line). The measurements were performed at a sweep rate of 5 °C min^{-1} from ambient temperature to 750 °C under air. Compared with MWCNT, the combustion peak of carbon is reduced in the $Li_{2.9}V_{1.9}Ti_{0.1}(PO_4)_3$/MWCNT composite. (c) XPS spectra for as prepared $Li_{2.9}V_{1.9}Ti_{0.1}(PO_4)_3$/MWCNT (X = 0.1) composites (C1s and P2p). No peaks responsible for C-V or C-P bonds are observed, indicating that the materials are just a composite of two phases, LVP and MWCNT.
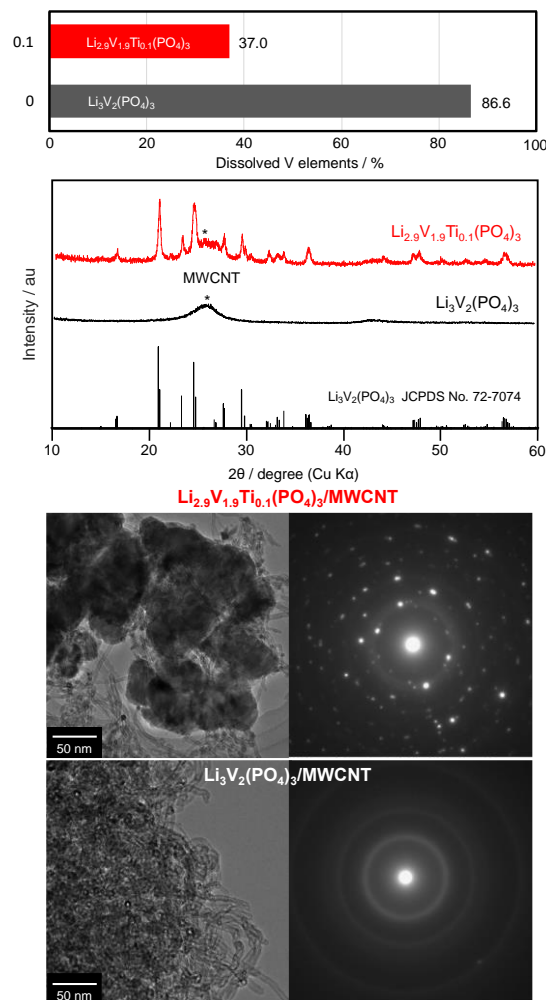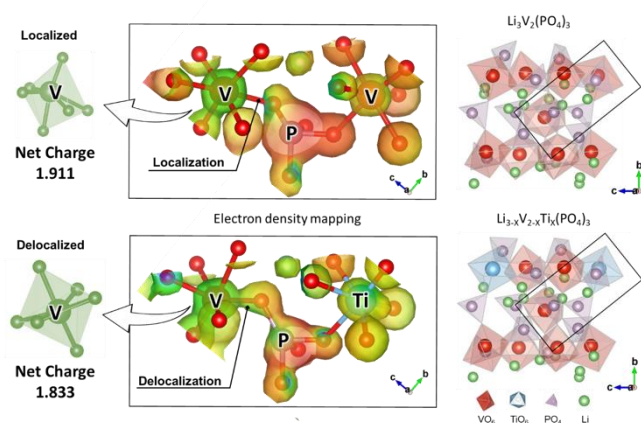
Fig.9 (left) Electron density map of $Li_3V_2(PO_4)_3$ and $Li_{2.8}V_{1.8}Ti_{0.2}(PO_4)_3$ calculated by the DV-Xα method. (Right) Cluster model for DV-Xα calculation of $Li_3V_2(PO_4)_3$ and $Li_{3-x}V_{2-x}Ti_x(PO_4)_3$. Compared with $Li_3V_2(PO_4)_3$, the electron density between V^{3+} and O^{2-} increased in $Li_{2.8}V_{1.8}Ti_{0.2}(PO_4)_3$, indicating suppression in the localization of electrons at V-O bonds.

filtrate after the soaking test in Ti-LVP (X = 0.1), with 36.98% of vanadium in as-prepared Ti-LVP dissolved from the crystals. Ti-LVP crystals were also observed in the TEM images and ED even after immersion in hot water. These results indicate that substituting titanium significantly suppresses vanadium dissolution from LVP crystals into polar solvents.

The suppression of vanadium dissolution in Ti-LVP is expected to be due to a modification of the ionicity of the V-O bond. We employed the DV-Xα method for molecular orbital calculation to determine the net charge of vanadium and the electron density of the V-O bond in LVP. The net charge of $Li_3V_{1.8}Ti_{0.2}(PO_4)_3$ (1.833) was lower than that of $Li_3V_2(PO_4)_3$ (1.911), indicating that the ionicity of the V-O bond was weakened by Ti^{4+} substitution. The electron density between V^{3+} and O^{2-} increased in $Li_3V_{1.8}Ti_{0.2}(PO_4)_3$ compared with that in $Li_3V_2(PO_4)_3$, indicating that the localization of electrons at V-O bonds is suppressed, as shown in Fig. 9. Typically, the electron density of the V-O bond in LVP is localized by the inductive effect of the PO_4 unit, forming a highly ionic bond.[44] We found that substituting V^{3+} with electronegative Ti^{4+} mitigates the inductive effect of P-O bond, delocalizing electrons at V-O bonds. This change in the ionicity of the V-O bond could have reduced reactivity with polar solvents, thereby preventing the dissolution of vanadium.

Ti-LVP also achieved nano-level modification of the LVP surface morphology. HRTEM image of $Li_{2.9}V_{1.9}Ti_{0.1}(PO_4)_3$ particles showed lattice fringes observed in particles corresponding to the *d* spacing of $Li_{2.9}V_{1.9}Ti_{0.1}(PO_4)_3$, as shown in Fig. S5. HRTEM images also revealed a clear difference in the surfaces of nanoparticles with or without Ti^{4+} substitution. A 3 nm layer was formed on the surface of nanoparticles where x ≥ 0.1. In contrast, such a surface phase was not clearly identified on the surface of $Li_3V_2(PO_4)_3$ nanoparticles. Interestingly, the observed surface layers consisted of an outer stacked phase and an inner amorphous phase, both approximately 1–2 nm thick. EDX showed a carbon peak on the surface of particles, suggesting that the outer stacking carbon was derived from chelating agents such as ethylene glycol and citric acid. The
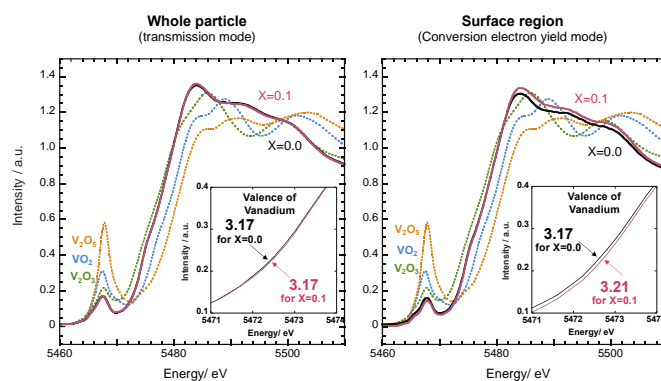

Fig. 10 V K-edge XANES spectra of as-prepared $Li_{3-x}V_{2-x}Ti_x(PO_4)_3$ /MWCNT for X = 0.0 and 0.1, and the V_2O_3, VO_2, and V_2O_5 reference spectra. The XANES measurement is conducted using transmission (featuring whole material) and conversion electron yield (featuring surface region: 20–40 nm), respectively. In the transmission mode, there is no change in the position of the XANES peak in either sample. In contrast, in the conversion electron yield mode, the XANES peak shifts to the high energy side for X = 0.1 compared with that for X = 0.0. The valence fitting using the reference shows that for X = 0.0, the valence of vanadium is 3.17 in the whole particle as well as surface regions. In contrast, the vanadium valence for X = 0.1 was 3.17 in the whole particle and 3.21 in the surface region, indicating an increase in vanadium valence in the surface region.

compositions of the inner amorphous phase and the inside of the crystals were almost the same (Fig. S6). To determine the valence state of vanadium in the surface amorphous phase, V K-edge spectra of $Li_{3-x}V_{2-x}Ti_x(PO_4)_3$/MWCNT for X = 0.0 and 0.1 were measured via XAFS transmission and conversion electron yield methods (Fig. 10). Note that the transmission method provides the oxidation state of vanadium over the entire particle. In contrast, the conversion electron yield method provides the valence state at the particle surface (20–40 nm)[47]. The XANES spectra of the V-K edge obtained by the transmission method were in perfect agreement between X = 0.0 and 0.1. The conversion electron yield method revealed a slight shift to the higher energy side for X = 0.1 than for X=0. The valence of
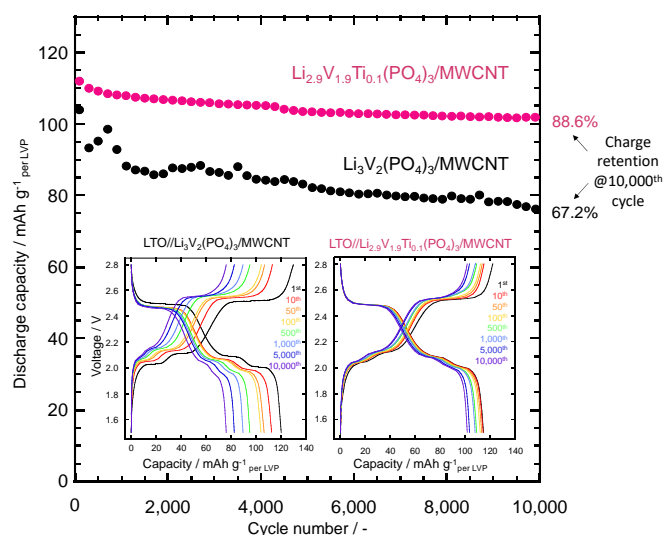

Fig.11 Plots of capacity against the cycle of LTO//($Li_{3-x}V_{2-x}Ti_x(PO_4)_3$(x = 0 and 0.1) full cells. LTO//$Li_{3-x}V_{2-x}Ti_x(PO_4)_3$(x = 0 and 0.1) full cells significantly improved the capacity retention after 10,000 cycles to 88.6% and 67.2%, respectively. Charge discharge curves of LTO//$Li_{3-x}V_{2-x}Ti_x(PO_4)_3$/MWCNT(x = 0 and 0.1) full-cells. For X = 0.0, the low-potential plateau (0.5Li$^+$, 2.02 V) decreases continuously, and this plateau almost disappears after 10,000 cycles. For X = 0.1, there is no marked change in the charge/discharge curve after 10,000 cycles.
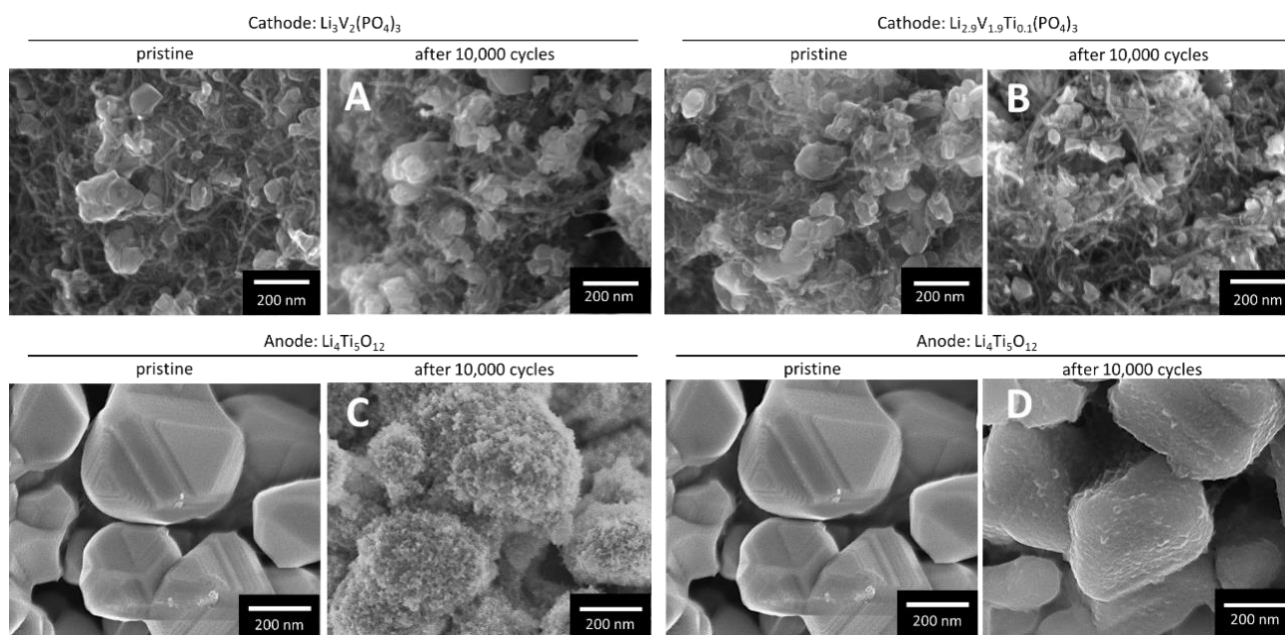
Fig.12 (SEM images of the surfaces of the anode ($Li_4Ti_5O_{12}$:LTO) and cathode ($Li_3V_2(PO_4)_3$ and $Li_{2.9}V_{1.9}Ti_{0.1}(PO_4)_3$) after cycling 10,000 cycles with a full cell described in the experimental section. Comparing images A and B, minor changes were observed from the initial prissiness stage. The LTO anode surfaces showed different levels of morphological change after 10,000 cycles. As shown in C, a substantial flake-shaped SEI cover is observed all over the LTO particles. However, as shown in D, a considerably low SEI accumulation is observed. The same anode surface was completely different from the combined cathode material for full-cell testing, and these differences require further discussion in relation to the substituted amount of Ti in the cathodic crystal.

vanadium was calculated by peak fitting using V_2O_3, VO_2, and V_2O_5 as references to the obtained XANES peaks, resulting in valence values of +3.17 (X = 0) and +3.21 (X = 0.1) for the conversion electron yield method, indicating that X = 0.1 was higher than X = 0. The combination of the TEM observation and XAFS measurement suggests that the surface amorphous phase (thickness 1–2 nm) at X = 0.1 contains a high valence of vanadium, such as V^{4+} and V^{5+}. These valence states are more electronegative than the vanadium valence found in LVP, which is V^{3+} (V^{3+} = 1.545, V^{4+} = 1.795, V^{5+} = 2.030).[34] Therefore, the electrons of O^{2-} are attracted to V^{4+} or V^{5+} in the V-O bonding of the surface amorphous phase, forming covalent V-O bonds and suppressing the vanadium dissolution. These results revealed two factors that diminished vanadium dissolution from LVP by Ti^{4+} doping. First, the ionicity of the V-O bonds decreases due to the relaxation of the inductive effect of the P-O bonds in the LVP crystal upon substituting Ti^{4+}. Second, an amorphous phase with highly covalent V-O bonds (1–2 nm in size) is formed on the surface of Ti-LVP particles.

Mechanism of improved full cell cycle performance with Ti-LVP

The previous section highlighted the inhibition of vanadium dissolution into polar solvents in Ti-LVP. This section explores the mechanism underlying the enhancement in cycle characteristics in full cells utilizing Ti-LVP. Fig. 11 shows the results of cycling tests at a C-rate of 10C on the LTO//LVP full cell constructed with $Li_3V_2(PO_4)_3$ and $Li_{2.9}V_{1.9}Ti_{0.1}(PO_4)_3$ as the cathode. The capacity retention for LTO//$Li_3V_2(PO_4)_3$ full cell decreased to 77% after 10,000 cycles. The charge–discharge curve for LTO//$Li_3V_2(PO_4)_3$ full cell during cycling shows that the low-potential plateau (0.5Li^+, 2.02 V) decreases continuously.

This plateau almost disappeared after 10,000 cycles. The decrease in capacity over the cycles was caused by the shift in the state-of-charge (SOC) between the cathode LVP and the anode LTO due to the formation of deposits by electrolyte decomposition on the anode accelerated by vanadium dissolved from LVP.[9] In contrast, LTO//$Li_{2.9}V_{1.9}Ti_{0.1}(PO_4)_3$ full cell exhibited superior capacity retention of 88.6% after 10,000 cycles. Unlike the LTO//$Li_3V_2(PO_4)_3$ full cell, the low-potential plateau was still observed in the charge–discharge curve after 10,000 cycles, indicating that the SOC shift in the full cell was successfully suppressed. Indeed, in Li-metal half cells (Li//$Li_3V_2(PO_4)_3$ and Li//$Li_{2.9}V_{1.9}Ti_{0.1}(PO_4)_3$) with cathodes after cycle tests, Li//$Li_{2.9}V_{1.9}Ti_{0.1}(PO_4)_3$ exhibited a lower initial voltage than Li//$Li_3V_2(PO_4)_3$ (Fig. S7), suggesting that the SOC shift in full cells with LTO//$Li_{2.9}V_{1.9}Ti_{0.1}(PO_4)_3$ full cell was suppressed. Ti-LVP showed improved capacity retention even at a lower C-rate of 0.5C: 75.1% for the LVP full cell and 92.1% for the Ti-LVP full cell at 50 cycles (Fig. S8). The coulombic efficiency was also higher for Ti-LVP than for LVP at all cycles. The capacity degradation due to the shift in the state of charge between the cathode and anode was observed in the LVP full cell. On the other hand, the charge-discharge profile of the Ti-LVP full cell did not change during cycling. These results at low C-rates of 0.5C were in good agreement with those at high rates of 10C. In addition to the excellent cycle performance described above, LTO//$Li_{2.9}V_{1.9}Ti_{0.1}(PO_4)_3$ exhibited an outstanding rate performance, as shown in Fig. S9. For LTO//$Li_{2.9}V_{1.9}Ti_{0.1}(PO_4)_3$, the capacity retention at 480C was 65.8%, which was significantly better than that of LTO//$Li_3V_2(PO_4)_3$(47.0%). This enhanced rate performance can be attributed to two factors: 1) improvement in electronic conductivity due to the mitigation of

inductive effects from Ti^{4+} doping and 2) enhancement in Li^+ diffusion via the formation of vacancies at Li sites.[31]

To verify the suppression of electrolyte decomposition on the electrodes after 10,000 cycles of the full cell, SEM observations and XPS analysis were conducted. Fig. 12 shows the SEM observation of the anode LTO after 10,000 cycles of the full cell. SEM images of the anode LTO revealed the presence of flake-shaped compounds on the surface when LVP was used as the cathode, in contrast to the smooth surface of the pristine LTO. A considerably lower accumulation of SEI was observed in the LTO using $Li_{2.9}V_{1.9}Ti_{0.1}(PO_4)_3$ as the cathode. The XPS results on the surface of LTO after cycling showed C-O, COO, and CO_3 shoulders corresponding to electrolyte decomposition products, in addition to the C-C peaks observed in the conductive agent (Fig. S10). In LTO using $Li_{2.9}V_{1.9}Ti_{0.1}(PO_4)_3$ as the cathode, the relative intensity of the peaks derived from electrolyte decomposition products, such as LiF, was lower than the peak corresponding to CF_2 derived from the binder in F1s spectra. These results were consistent with the decrease in electrolyte decomposition in SEM images using $Li_{2.9}V_{1.9}Ti_{0.1}(PO_4)_3$ as a cathode. The peak corresponding to V^{5+} in the V2p spectrum was observed when using either $Li_3V_2(PO_4)_3$ or $Li_{2.9}V_{1.9}Ti_{0.1}(PO_4)_3$ as the cathode. To quantify the amount of vanadium ions dissolved after the cycle test, an ICP-MS measurement was performed. The amount of vanadium ions on the LTO surface using $Li_{2.9}V_{1.9}Ti_{0.1}(PO_4)_3$ as a cathode was 1.9 μg, lower than 3.4 μg in the case of $Li_3V_2(PO_4)_3$ (Table S3). These results indicate that $LTO//Li_{2.9}V_{1.9}Ti_{0.1}(PO_4)_3$ exhibits high cycle performance due to the suppression of vanadium dissolution and electrolyte decomposition on the anode, suppressing the gradual SOC shift during cycling.

Conclusion

In conclusion, we successfully synthesized highly dispersed $Li_3V_2(PO_4)_3$ (LVP) composites through stoichiometric substitution of various metals (Ti^{4+}, Al^{3+}, Mn^{2+}) with monoclinic LVP. Among the metal-doped LVPs, Ti-LVP demonstrated the best cycle performance, retaining 88.6% of its capacity over 10,000 cycles in full cells. A detailed investigation of $Li_{3-x}V_{2-x}Ti_x(PO_4)_3$ with Ti^{4+} doping (X = 0–0.2) revealed selective Ti^{4+} substitution in V^{3+} at the V(1) site and the formation of vacancies at the Li(2) site. Vanadium dissolution tests under extreme conditions with warm water showcased the high stability of Ti-LVP compared with LVP. Molecular orbital calculations indicated a delocalized electron density of the V-O bonds in the bulk of Ti-LVP, reducing ionicity. Additionally, Ti-LVP formed a thin amorphous phase of 1–2 nm with V^{4+} or V^{5+} on the surface of the particles, effectively diminishing the dissolution of vanadium ions. Combined SEM observations, XPS, and ICP-MS measurements of the full cell after cycling tests demonstrated that Ti-LVP exhibited high cycle performance by suppressing vanadium ion dissolution. This suppression, in turn, mitigated electrolyte decomposition on the anode, leading to the suppression of the state-of-charge shift between the cathode and anode. These findings provide valuable insights into addressing challenges related to the dissolution of transition metals in energy storage devices.

Author Contributions

The manuscript was written through the contributions of all authors. All authors have given approval to the final version of the manuscript.

Conflicts of interest

The authors declare no conflict of interest.

Acknowledgments

References

1   M. S. Whittingham, *Chem. Rev.*, 2004, **104**, 4271–4301.
2   Q. Zhu, J. Li, P. Simon and B. Xu, *Energy Storage Materials*, 2021, **35**, 630–660.
3   N. Okita, E. Iwama and K. Naoi, *Electrochemistry*, 2020, **88**, 83–87.
4   X. Rui, Q. Yan, M. Skyllas-Kazacos and T. M. Lim, *J. Power Sources*, 2014, **258**, 19–38.
5   M. Onoda and H. Hirose, *J. Phys. Soc. Jpn.*, 2012, **81**, 094801.
6   A. Tang, X. Wang, G. Xu, R. Peng and H. Nie, *Mater. Lett.*, 2009, **63**, 2396–2398.
7   S.-C. Yin, P. S. Strobel, H. Grondey and L. F. Nazar, *Chem. Mater.*, 2004, **16**, 1456–1465.
8   K. Naoi, K. Kisu, E. Iwama, Y. Sato, M. Shinoda, N. Okita and W. Naoi, *J. Electrochem. Soc.*, 2015, **162**, A827.
9   N. Okita, E. Iwama, S. Tatsumi, T. N. H. Võ, W. Naoi, M. T. H. Reid and K. Naoi, *Electrochemistry* , 2019, **87**, 148–155.
10   Y. Chikaoka, R. Okuda, E. Iwama, M. Kuwao, W. Naoi and K. Naoi, *Electrochemistry* , 2021, **89**, 204–210.
11   S. Komaba, N. Kumagai and Y. Kataoka, *Electrochim. Acta*, 2002, **47**, 1229–1239.
12   C. Zhan, T. Wu, J. Lu and K. Amine, *Energy Environ. Sci.*, 2018, **11**, 243–257.
13   M. A. Cambaz, B. P. Vinayan, S. A. Pervez, R. E. Johnsen, H. Geßwein, A. A. Guda, Y. V. Rusalev, M. K. Kinyanjui, U.

Kaiser and M. Fichtner, *Chem. Mater.*, 2019, **31**, 7941–7950.

14   J. A. Gilbert, I. A. Shkrob and D. P. Abraham, *J. Electrochem. Soc.*, 2017, **164**, A389.

15   C. Zhan, J. Lu, A. Jeremy Kropf, T. Wu, A. N. Jansen, Y.-K. Sun, X. Qiu and K. Amine, *Nat. Commun.*, 2013, **4**, 2437.

16   C. Zhan, X. Qiu, J. Lu and K. Amine, *Adv. Mater. Interfaces*, 2016, **3**, 1500856.

17   Z. Song, K. Feng, H. Zhang, P. Guo, L. Jiang, Q. Wang, H. Zhang and X. Li, *Nano Energy*, 2019, **66**, 104175.

18   T.-F. Yi, Y.-R. Zhu, X.-D. Zhu, J. Shu, C.-B. Yue and A.-N. Zhou, *Ionics* , 2009, **15**, 779–784.

19   A. Zhu, J. Wu, B. Wang, J. Zhou, Y. Zhang, Y. Guo, K. Wu, H. Wu, Q. Wang and Y. Zhang, *ACS Appl. Mater. Interfaces*, 2021, **13**, 61248–61257.

20   C. Yin, X. Wen, L. Wan, Z. Shi, Z. Wei, X. Li, Q. Gu, B. Qiu and Z. Liu, *J. Power Sources*, 2021, **503**, 230048.

21   A. Gutierrez and A. Manthiram, *J. Electrochem. Soc.*, 2013, **160**, A901.

22   Y.-S. Lee, N. Kumada and M. Yoshio, *J. Power Sources*, 2001, **96**, 376–384.

23   H. Sclar, O. Haik, T. Menachem, J. Grinblat, N. Leifer, A. Meitav, S. Luski and D. Aurbach, *J. Electrochem. Soc.*, 2011, **159**, A228.

24   K. A. Walz, C. S. Johnson, J. Genthe, L. C. Stoiber, W. A. Zeltner, M. A. Anderson and M. M. Thackeray, *J. Power Sources*, 2010, **195**, 4943–4951.

25   S.-C. Park, Y.-M. Kim, S.-C. Han, S. Ahn, C.-H. Ku and J.-Y. Lee, *J. Power Sources*, 2002, **107**, 42–47.

26   D.-Q. Liu, X.-Q. Liu and Z.-Z. He, *Mater. Chem. Phys.*, 2007, **105**, 362–366.

27   J. Cao, G. Cao, H. Yu, J. Xie and X. Zhao, *Rare Met.*, 2011, **30**, 39–43.

28   R. Vidu and P. Stroeve, *Ind. Eng. Chem. Res.*, 2004, **43**, 3314–3324.

29   C. Qing, Y. Bai, J. Yang and W. Zhang, *Electrochim. Acta*, 2011, **56**, 6612–6618.

30   D. Liu, Z. He and X. Liu, *Mater. Lett.*, 2007, **61**, 4703–4706.

31   Q. Wang, H. Huo, Z. Lin, Z. Zhang, S. Wang, X. Yin, Y. Ma, P. Zuo, J. Wang, X. Cheng, C. Du, Y. Gao and G. Yin, *ACS Appl. Energy Mater.*, 2020, **3**, 715–722.

32   M. Bini, S. Ferrari, D. Capsoni and V. Massarotti, *Electrochim. Acta*, 2011, **56**, 2648–2655.

33   L. Li, C. Fan, T. Zeng, X. Zhang, W. Zhang and S. Han, *J. Alloys Compd.*, 2015, **650**, 136–142.

34   K. Li and D. Xue, *J. Phys. Chem. A*, 2006, **110**, 11332–11337.

35   E. Iwama, N. Kawabata, N. Nishio, K. Kisu, J. Miyamoto, W. Naoi, P. Rozier, P. Simon and K. Naoi, *ACS Nano*, 2016, **10**, 5398–5404.

36   E. Iwama, P. Simon and K. Naoi, *Current Opinion in Electrochemistry*, 2017, **6**, 120–126.

37   A. Rosén, D. E. Ellis, H. Adachi and F. W. Averill, *J. Chem. Phys.*, 1976, **65**, 3629–3634.

38   Y. Ito, Y. Idemoto, K. Ui and N. Koura, *Electrochemistry* , 2003, **71**, 1145–1147.

39   T. Watanabe, N. Wakiyama, A. Kusai and M. Senna, *Powder Technol.*, 2004, **141**, 227–232.

40   D. Okada, F. Nakano, K. Uematsu, H. Okawa, A. Itadani, K. Toda and M. Sato, *Electrochemistry* , 2015, **83**, 828–830.

41   X. Cui and T. Liu, *Ionics* , 2019, **25**, 3603–3609.

42   H. Huang, S.-C. Yin, T. Kerr, N. Taylor and L. F. Nazar, *Adv. Mater.*, 2002, **14**, 1525–1528.

43   D. Morgan, G. Ceder, Saïdi, J. Barker, J. Swoyer, H. Huang and G. Adamson, *Chem. Mater.*, 2002, **14**, 4684–4693.

44   S.-C. Yin, H. Grondey, P. Strobel, M. Anne and L. F. Nazar, *J. Am. Chem. Soc.*, 2003, **125**, 10402–10411.

45   H. Huo, Z. Lin, G. Zhong, S. Lou, J. Wang, Y. Ma, C. Dai, Y. Xiong, G. Yin and Y. Yang, *J. Mater. Chem. A Mater. Energy Sustain.*, 2022, **67**, 593–603.

46   A. Mondal and M. Kaupp, *Solid State Nucl. Magn. Reson.*, 2019, **101**, 89–100.

47   W. T. Elam, J. P. Kirkland, R. A. Neiser and P. D. Wolf, *Phys. Rev. B Condens. Matter*, 1988, **38**, 26–30.